Deformation of porous flexible strip in low and moderate Reynolds number flows

M. Pezzulla [1,*] E. F. Strong,[2] F. Gallaire,[3] and P. M. Reis [1]

[1] *Flexible Structures Laboratory, École Polytechnique Fédérale de Lausanne, 1015 Lausanne, Switzerland*

[2] *University of Colorado Boulder, Boulder, Colorado 80309, USA*

[3] *Laboratory of Fluid Mechanics and Instabilities, École Polytechnique Fédérale de Lausanne, 1015 Lausanne, Switzerland*

(Received 16 April 2020; accepted 27 July 2020; published 21 August 2020)

We present results from a combined experimental and numerical investigation of the fluid-structure interaction of cantilevered porous flexible strips, towed through a fluid bath. We characterize the steady-state deformation of the strips and their associated drag, focusing on the low and moderate Reynolds (Re) number regimes. Our microfabricated strips offer independent control over porosity and permeability, a feature not available in previous studies. We fabricate strips with different levels of permeability, spanning over two orders of magnitude, while fixing their porosity at 50%. Then, the vertically clamped porous strips are towed inside a viscous bath. In parallel to the experiments, we model the strip as an *elastica* that is loaded locally by low (or moderate) Reynolds forces, via local drag coefficients. At low Re, we find that the drag coefficient, which can be obtained from Stokes simulations of rigid strips under perpendicular flow, varies with permeability by less than 10%. By contrast, at moderate Re, the drag coefficient depends significantly and nonmonotonically on permeability. Whereas porosity dictates the drag coefficient at low Re, our results demonstrate that a precisely designed permeability plays a major role at moderate Re, enabling large variations of the drag coefficients at a set level of porosity. Since porosity is directly linked to weight via the density of the effective solid, understanding how porous structures of fixed porosity and varying permeability interact with the surrounding fluid is of relevance to flying insects and microdrones.

DOI: 10.1103/PhysRevFluids.5.084103

I. INTRODUCTION

From bacteria, insect wings and plants to bridges and airplanes, the interactions between flexible structures and viscous fluids occur over a wide range of length scales and Reynolds numbers (Re). The study of fluid-structure interactions (FSI) is an area of intense research, including bending of fibers in microfluidic channels [1], insect [2,3] and bird flight [4], bacterial [5] and fish locomotion [6], flapping flags [7,8], plant motion [9], wind turbines [10], aeroelastic instabilities of bridges [11], and flight vehicle aerodynamics [12]. All these studies evidence several of the most challenging features of FSI problems arising from the nonlocal and nonlinear coupling between the elasticity of the structure and the fluid flow, translating into balance equations that are integro-differential [13].

Given the inherent complexity of FSI problems, early efforts to study the fluid loading of porous structures have tended to focus on the rigid case, thus excluding deformation. Not only was this approach motivated by the reduced level of difficulty for rigid structures, but it was also of technical relevance for filters and porous media. Indeed, starting from the pioneering works by Darcy [14]

*Corresponding author: matteo.pezzulla@epfl.ch

on the flow through sand (which led to a law known today as Darcy's law) and Brinkman [15] who extended this law to include viscous effects, the interactions between rigid porous structures and fluids have been at the core of many experimental and numerical investigations. Examples of studies in this class of problems include the terminal velocity of porous spheres [16,17], the drag on rigid annuli [18] and porous cylinders [19], and the flow through and around porous plates [20]. More recently, the drag on two-dimensional (2D) porous plates has been studied via numerical models that propose a modified Darcy-Brinkman formulation, where the flow inside the porous media is described via the Darcy-Brinkman equations and the flow outside of the body is described via the incompressible Navier-Stokes equations [21,22]. In this case, the porous microstructure of the body is represented by the so-called Darcy number, Da, defined as the ratio between the permeability k of the medium (which quantifies the density, connectivity, and tortuosity of the porous structure) and a characteristic area of the body. The determination of the permeability, and consequently of the Darcy number, is typically accomplished either via empirical relations, or physics-based models such as the Carman-Kozeny equations [23,24], or measured in independent experiments.

More specifically, the study described in Ref. [21] has provided understanding on how the drag coefficient of a porous (homogenized) plate is a nonmonotonic function of the Darcy number for moderate Reynolds numbers, starting from 0 in the limit of $\mathrm{Da} \to 1$ (completely porous structure), and increasing up to the drag coefficient of the equivalent nonporous plate in the limit of $\mathrm{Da} \to 0$. In between these two extreme values of Da, the drag coefficient reaches a maximum that moves towards smaller Darcy numbers as Re is decreased, while this peak vanishes for Stokes flows. These findings are reminiscent of the numerical results reported in Ref. [19], where the drag coefficient of a porous cylinder is also shown to have a maximum for a particular value of the Darcy number, which depends on Re. While numerical simulations [19,21] suggest the occurrence of an overshoot of the drag coefficient (i.e., the possibility for a porous structure to have a drag coefficient larger than that for the equivalent nonporous structure) there is a lack of experimental results due to the required high level of precision in the fabrication of porous structures with finely controlled porosity and, most importantly, a custom-defined permeability. A few experimental studies have been performed on rigid porous structures. For example, in Ref. [25], the drag on rigid plates in either perpendicular or parallel flow was studied via the measurement of their sedimentation velocity. In Ref. [26] the drag coefficient of porous rigid disks with a fixed porosity and different permeabilities was evaluated via dragging experiments and direct force measurements, for small Re numbers up to $\mathrm{Re} = 10$. In this latter study, the drag coefficient was shown to depend monotonically on permeability, in agreement with the theoretical, numerical, and experimental findings for an annulus in Stokes flow [18]. More importantly, their findings demonstrated that an annulus with a porosity of 80%, immersed in a Stokes flow, has a drag coefficient that is only 20% smaller than that of the equivalent nonporous disk. This is a key feature of Stokes flows, where the fluid has such small inertia that is essentially unable to pass through the porous structure, which is therefore almost seen as nearly nonporous. For higher values of Re, the drag coefficient becomes a strong (possibly nonmonotonic) function of permeability [18].

FSI studies on structures that are porous and deformable have biological relevance. For example, the wings of the fairy fly [3] and biological filters such as those found in a phloem sieve plate [27] are, indeed, both flexible and porous. Depending on whether the structure-fluid coupling takes place at low Re (Stokes flows) or moderate Re numbers, natural designs (in terms of geometric and material properties) can vary considerably. For instance, the dragonfly [2] has developed a nonporous wing structure with a venation network that endows the wing with a nonuniform bending stiffness to optimize its flight efficiency at moderate Re ($\approx$2000–5000). By contrast, the fairy fly [3] has developed porous wings with bristles emanating from an inner core to reduce weight, while maintaining the required lift for its flight at low Re (≈ 10). For these two specific cases, it is still unclear what are the underlying physical mechanisms that rationalize the specific differences in their designs; past research efforts have focused on parametric studies without taking into account constraints that are important for insect flight, such as weight.

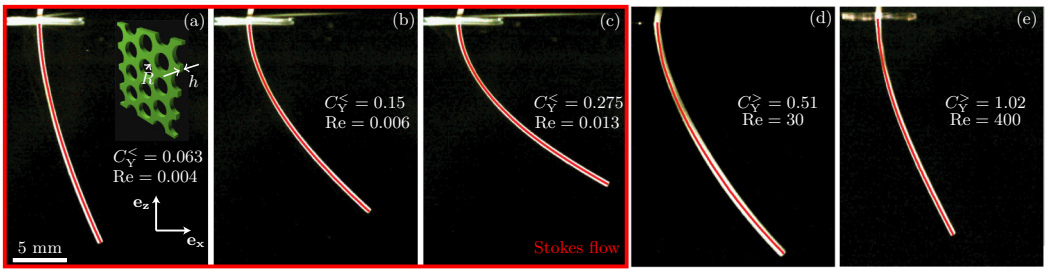

FIG. 1. Experimental and numerical shapes of a porous strip at different Re and Ca ($\mathrm{Da} = 2 \times 10^{-4}$). (a)–(c) Low Reynolds flows, the strip increases its deflection as the Cauchy number increases. The numerical results (in red) obtained by determining the local drag coefficients by fitting the numerical shape to experiments (Sec. III), describe well the experiments (Sec. II). The inset in (a) shows a schematic of a representative porous membrane, depicting the relevant geometric parameters. (d), (e) Deflection of a porous strip at moderate Reynolds number, the reduced numerical model fits well the experimental shapes.

The aim of the present investigation is to study the drag and the deformation of a simplified prototypical physical model of a porous flexible structure: a porous strip, at fixed weight conditions, with constant porosity ϕ (defined as the ratio between the projected area of the porous strip over the area of a strip with no holes [28]). Experiments on flexible porous strips at high Re ($\mathrm{Re} \simeq 5000$) were reported in Ref. [29], with drag coefficients measured to be nearly the same as that for the equivalent rigid strip, over a wide range of porosities. However, the perforated strips comprised a fixed number of holes arranged in a hexagonal array. Therefore, values of porosity were targeted by changing the radii of the holes, inevitably accompanied by a simultaneous change of permeability related to the typical size of the holes.

Computing permeability involves the quantification of the pressure drop across the membrane for a given flow rate. For a rigid membrane with a hexagonal array of holes, the permeability can be calculated analytically by taking into account the pore size distribution, the finite thickness of the membrane and the pore-pore interaction [27]. Starting from a membrane with just one hole at low Reynolds, Dagan *et al.* [30] showed that the superposition of the pressure drops corresponding to the Sampson's solution for zero thickness and the Poiseuille's solution for finite thicknesses introduces errors that are at most 1% with respect to the numerical solutions. Then Jensen *et al.* [27] considered the pore-pore interaction, introducing a correction factor c_{corr} that depends on the array of the holes. For a rigid membrane of thickness h, with a hexagonal array of holes with radius R and porosity ϕ, as the one depicted in the inset of Fig. 1(a), the permeability can be expressed as [27]

$$k = \phi \frac{Rh}{3\pi c_{\mathrm{corr}} + 8h/R}, \tag{1}$$

where $c_{\mathrm{corr}} = 1 - 2.3(\phi\sqrt{3}/2\pi)^{3/2}$ for a hexagonal array of holes. Using this definition for k, the Darcy number can be expressed as

$$\mathrm{Da} = \frac{k}{Lb}, \tag{2}$$

where L denotes the length of the membrane and b its width, so that the total area Lb is taken as the characteristic area. Taking Eq. (2) to estimate the permeability of the porous strips studied experimentally in Ref. [28,29] and theoretically (for the rigid case) in Ref. [31], we find that the investigated specimens had different values for both the porosity and the permeability, making it difficult to distinguish the individual contributions of the two effects on the drag. For example, as stated previously, had the porosity been constant for all of the strips tested, it would have been possible to draw conclusions on the sole effect of permeability on strips that share the same weight (same porosity), which remains unclear.

Here we study the deformation induced by the fluid loading on porous flexible strips that share the same porosity (i.e., weight), in three different ranges of Reynolds numbers. We perform a combination of towing experiments in a fluid tank, computer simulations using a reduced structural mechanics model of the strips, and Stokes simulations for the low Re regime. We denote the fluid density by ρ_f, the dynamic viscosity as μ, the free stream (or towing) velocity by U, the length of the strips by L, and define the Reynolds number as

$$\mathrm{Re} = \frac{\rho_f U L}{\mu}, \tag{3}$$

which we vary over three ranges $\mathrm{Re} \in (0.001, 0.01)$, $\mathrm{Re} \in (10, 60)$, and $\mathrm{Re} \in (400, 800)$, by systematically varying the value of towing velocity U and using three different fluids in the tank. During each towing experiment, we set the parameters such that the tip of the strip does not rotate by more than 45°, a value above which tangential forces, which are not modeled in our reduced inextensible elastica model, are not negligible. To investigate the role of the permeability, k, we fix the value of porosity at 50% and microfabricate nine elastomeric porous strips with precisely controlled values of k. To characterize the mechanical properties of the fabricated samples, we perform cantilever tests and measure their bending stiffness B, which does not vary with permeability. This means that, for the same towing velocity, the difference in the deformation of two different strips can be attributed to different interactions with the fluid. Given that there are two types of forces at play in this class of FSI systems, namely elastic and fluid forces, it is customary to distinguish between two regimes where one force predominate over the other. The Cauchy number, a dimensionless quantity, is typically introduced to denote the ratio of these two force scales. By modeling the strip as a bending beam, we can estimate the elastic forces to scale as B/L^2. On one hand, for low Re flows, where fluid forces scale linearly with the velocity via the dynamic viscosity, the corresponding Cauchy number is defined as

$$C_Y^{<} = \frac{\mu U L^3}{2B}. \tag{4}$$

On the other hand, for moderate Re flows, where the aerodynamic forces scale with the dynamic pressure, the corresponding Cauchy number is defined as

$$C_Y^{>} = \frac{\rho_f U^2 b L^3}{B} = 2\mathrm{Re}\frac{b}{L} C_Y^{<}. \tag{5}$$

In summary, the bending of porous strips under fluid loading is described by three dimensionless parameters: the Darcy number defined in Eq. (2), the Reynolds number defined in Eq. (3), and the Cauchy number, which takes a different form for the low or the moderate Re number regimes according to Eqs. (4) and (5), respectively.

As a preamble of our study (full details are provided throughout the paper), illustrative examples of our results are presented in Fig. 1, where we show photographs of the deformed shapes of a porous strip, at steady state, for different values of Reynolds, Cauchy, and Darcy numbers. Since the strips oscillate at equilibrium for moderate Re, we perform a time average over one period of oscillation and refer to the result as the steady-state shape. Specifically, Figs. 1(a)–1(c) show the increasing deformation of a porous strip for $\mathrm{Re} \in (0.001, 0.01)$, due to the increasing towing velocity (i.e., Cauchy number). We compare these experimental profiles with the numerical results from our reduced model (red lines superposed onto the photographs), which we use to find the local normal drag coefficient by looking for the best fit in a least-squares sense. Moreover, we perform Stokes simulations on the rigid strips in perpendicular flow to determine the normal drag coefficient, assuming this coefficient to be the local normal drag coefficient for deformable strips, similarly to what has been shown in Ref. [32], finding an excellent agreement with the experiments. Figures 1(d) and 1(e) show the experimental profiles, together with the numerically computed shape (red line), for $\mathrm{Re} = 30$ and $\mathrm{Re} = 400$, respectively. For these higher values of Re, the drag coefficient varies nonmonotonically with permeability, similarly to what has been found for rigid structures [19]. In

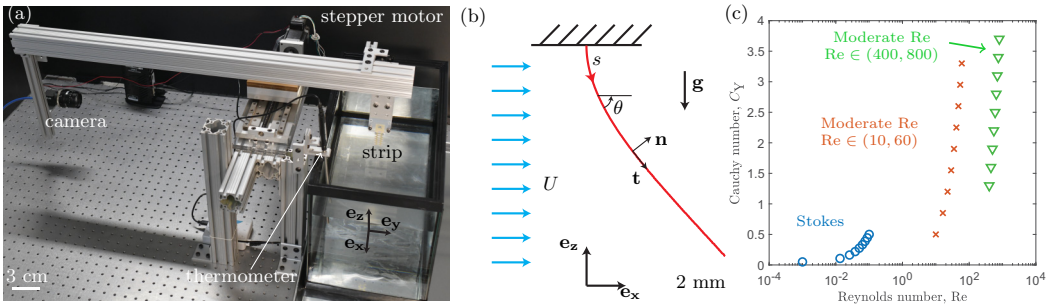

FIG. 2. (a) Experimental apparatus: the perforated strip specimens are immersed in a tank containing a viscous fluid and clamped onto a horizontal driving beam. This beam is translated by a motorized linear stage along $\mathbf{e}_x$. A camera is mounted onto the other extremity of the beam to image the deformed strip on its frame of reference during translation. (b) Representative example of equilibrium centerline (in red) of the porous strip extracted using image processing; the arc length coordinate is denoted as $s \in [0, 1]$. (c) Parameter space (Re, C_Y) explored in the experimental campaigns that we performed, with the Darcy number in the range $[2 \times 10^{-6}, 2 \times 10^{-4}]$ for each point shown in the plot.

terms of the deformed shape, this nonmonotonic drag translates into a *come-back* of the strips for decreasing Darcy numbers, as we will show in Fig. 10 via the fitted shapes. As summarized by Fig. 1, we seek to understand how permeability affects the drag and the deformation of porous flexible structures, at low and moderate Re, via a combination of experiments and computer simulations.

Our paper is organized as follows. In Sec. II we describe the experimental apparatus and protocol, together with the microfabrication technique followed to produce the porous strips, as well as their mechanical characterization. In Sec. III we present the reduced structural-mechanics model based on an *elastica* framework, in which we distinguish between the fluid loading at low and moderate Re. In Sec. IV we describe our protocol for the numerical simulations of Stokes equations in the case of rigid porous strips in perpendicular flow. We investigate how the local normal drag coefficient increases sharply near the tip of the strip, and how this might affect the bending deformations of the samples. Moreover, we quantify wall effects for different permeabilities. In Sec. V we present our results starting from low Re, for which we compare experiments and numerics in terms of tip displacement and local drag coefficient. We then turn to moderate Reynolds numbers, where we investigate how the local normal drag coefficient varies with permeability. Finally, we turn to the evaluation of the total drag force on the porous strips, therefore defining a global drag coefficient. In this way, we compare the drag on deformable strips with the drag on the rigid ones, in terms of the reconfiguration number. We provide a conclusion in Sec. VI.

II. THE EXPERIMENTS: TOWING A POROUS FLEXIBLE STRIP THROUGH A VISCOUS FLUID

In this section, we start by presenting the experimental apparatus used to tow a porous flexible strip through a bath of a viscous fluid. We then describe the experimental procedure that we followed to quantify the corresponding drag coefficients measured during towing. In Sec. II C we detail the microfabrication protocol used to produce our perforated strip specimens. Throughout, we performed three sets of experiments in the following ranges of Reynolds number: $\mathrm{Re} \in (0.001, 0.01)$, $\mathrm{Re} \in (10, 60)$, and $\mathrm{Re} \in (400, 800)$.

A. Experimental apparatus

In Fig. 2(a) we present a photograph of the experimental apparatus, comprising a horizontal aluminum beam mounted onto a motorized linear stage, which is itself driven by a stepper motor. This horizontal beam acts as a driver and can be made to translate along the $-\mathbf{e}_x$ direction,

with an imposed velocity in the range $0.3 \leqslant U\,[\mathrm{cm/s}] \leqslant 3$. For each experimental run, a porous flexible strip was clamped to one end of the driving beam, immersed in a parallelepipedic tank ($46 \times 26 \times 23\ \mathrm{cm}^3$) and towed at a set constant velocity. As detailed in Sec. II C, the porous strips were fabricated through casting using an elastomeric material, with the following dimensions: thickness $h = 400\,\mu\mathrm{m}$, width $b = 6.67\,\mathrm{mm}$, and length $L = 23.09\,\mathrm{mm}$. The strips were made porous by a hexagonal array of through holes with a void fraction that was fixed at $\phi = 0.5$, throughout. The permeability of the strips was systematically varied by the combined variation of the number and size of the holes in the pattern.

A thermometer was used to measure the temperature of the fluid in the tank to evaluate its viscosity for each experiment, thereby minimizing experimental uncertainties due to temperature fluctuations. More details on the three fluids that we used (distilled water and two different silicone oils) are given below. A color scientific camera (FLEA3 FL3, Edmund Optics) was mounted to the other end of the driving beam, enabling the imaging of the bending deformation of the strip in the x-z plane and in the moving frame of reference. A spotlight (SL-20LX, Sima Corp.) was attached next to the clamping mount of the specimen to enhance illumination and facilitate the extraction of the edge profile through image processing.

The experimental setup was computer controlled using LabView (National Instruments), which allowed for automation of the experimental runs at different towing velocities and synchronous imaging. For statistical purposes, we ran a sequence of 10 identical experiments at each value of the towing velocity, where we recorded a video of the deforming strip and measured the temperature of the fluid, while automatically turning off the camera and the thermometer during the repositioning step.

B. Experimental protocol

To vary the Reynolds number considerably, we performed the experiments using three different fluids: silicone oil Bluesil 47 V 1000 (Silitech, AG), silicone oil Bluesil 47 V 10 (Silitech, AG), and distilled water. As such, we could explore three different values of the dynamic viscosity of the fluid: 1 Pa s, 10^{-2} Pa s, and 10^{-3} Pa s, respectively. In Appendix A we provide details of the characterization of these fluids, which, in the explored ranges of experimental conditions, exhibit Newtonian behavior. We fixed the distance between the free surface of the fluid and the clamp to be zero, given that the results on the drag coefficients were unchanged if the distance was set anywhere between 0 and ≈ 3 mm. When the strips were immersed in the fluid bath, air could be trapped inside the holes and effectively increase the permeability of the samples. To ensure the permeability had the value targeted by design, we sprayed each strip with ethanol, shortly before immersing it into the bath (silicone oil or distilled water). Consequently, the ethanol completely filled the holes, effectively removing any residual air, eventually dissolving in the silicone oil or water once the strip was fully immersed.

For each towing experiment at a set value of the driving velocity U, the strip always reached a steady state; i.e., with a stationary shape in the moving frame of reference. To measure the drag coefficient for a given experiment, we first analyzed the acquired video, automatically searching for the steady-state portion by tracking the tip position, and extracting the corresponding edge profile of the strip in this steady regime through image processing. Representative examples of the deformation of the strip for different experimental conditions are presented in Fig. 1, where the profiles extracted through image processing (red lines) are superposed onto the corresponding original photograph. An example of an extracted profile is also shown in Fig. 2(b), where we superpose schematics of the relevant geometric quantities used in the upcoming analysis of this FSI problem, namely, the tangent and normal unit vectors ($\mathbf{t}$, $\mathbf{n}$), the arc length coordinate $s \in [0, 1]$, and the angle θ between the tangent vector and the $\mathbf{e}_x$ direction. In our experiments, the angle at the tip was never smaller than 45°, meaning that the tip of the strip does not rotate by more than 45°. Due to the distributed fluid loading, the elastic strip deforms in pure bending as a cantilever beam, such that its shape is uniform along the $\mathbf{e}_y$ direction (i.e., the strip is flat in this out-of-plane direction).

Consequently, we shall model the strip as a 1D inextensible beam, albeit with finite rotations—an *elastica*—as detailed in Sec. III.

For the experiments in creeping flow conditions (Re $\lesssim 1$), the equilibrium shape was decidedly steady; the strip was static in the moving frame of reference. However, for moderate Re ($\gtrsim$50), periodic oscillations were observed, most likely induced by some degree of vortex shedding and/or dynamic interactions with the walls of the fluid tank. For example, at Re = 350, we observed oscillations with a frequency $f = 1$ Hz, which corresponds to a Strouhal number of St $= fL/U \approx 1$ (taking the undeformed length of the strip, L as the characteristic length). This Strouhal number is much larger than, for example, the one corresponding to oscillating flows around a cylinder that is more around 0.1. Still, these oscillations remained small throughout with a maximum amplitude (at the tip) that was at most 5–10 times the thickness of the strip ($h = 400\,\mu$m), hence much smaller than the strip length ($L = 23.09$ mm). Given the small amplitude of these oscillations, and to facilitate the analysis, we averaged the shape of the strip over one period, and extracted the drag coefficient of the averaged shape. The image processing was carried out in MATLAB (Mathworks) using an in-house code.

In Fig. 2(c), we present a summary of the parameters that we explored, in the form of a parameter space within the domain (Re, C_Y). As detailed in the plot, each experimental range is labeled with referencing to the respective section where the experimental results are presented and discussed. In addition, we note that the Darcy number has been varied in the range $[2 \times 10^{-6}, 2 \times 10^{-4}]$ for each experimental point in the domain (all nine strips were tested at each pair of (Re, C_Y) values).

C. Microfabrication of the perforated strips

We have placed particular attention to the fabrication of our specimens to ensure high-quality experimental data. The fabrication protocol that we have developed enables the mechanical and geometrical properties of the porous strips to be set in an accurate, precise and reproducible manner. As described in Sec. I, we seek to study the effect of permeability, k [see Eq. (1)], as measured by the Darcy number [defined in Eq. (2)], on the deformation of porous strips, while fixing their porosity at $\phi = 0.5$. We chose a hexagonal array of circular holes, whose radii and number are changed concurrently to explore different levels of k, while maintaining the fixed level of ϕ. Hence, as indicated by Eqs. (1) and (2), strips with smaller and a higher number of holes have lower permeabilities. Considering the requirements on the ranges of Reynolds that we stated in the introduction, and the fact that we want our samples to be deformable, but only moderately so ($C_Y \simeq 1$), the length of the strip should remain $L \lesssim 5$ cm and the radii of the holes should be $R \lesssim 5$ mm, with a lower bound of 50 μm imposed by fabrication limits (more on this below).

Past work on the flow past flexible perforated strips at high-Re conditions [29] involved laser cutting of thin thermoplastic plates [polyethylene terephthalate glycol (PETG)]. Unfortunately, despite early diligent attempts, we could not use this convenient rapid-prototyping technique for the present study since we need to fabricate strips with holes much smaller than 2 mm (this was the minimum value explored in Ref. [29]). There are two reasons for this limitation. First, the resolution of our laser cutter was not sufficiently high to fabricate hexagonal patterns with a hole radius smaller than 1 mm. Second, melting of the plastic during cutting between two adjacent holes resulted in an uncontrollable degradation of the material properties, including a build-up of inhomogeneous residual stresses that compromised the reproducibility of the experiments.

Following an alternative point of departure, we fabricated elastomeric porous strips by casting them into microfabricated silicon molds using 100 mm silicon wafers and standard clean-room technology. As a word of caution, the entire procedure from a clean wafer to a high-precision usable mold can take up to 2 wk and be relatively expensive. These time and cost considerations motivated us to design a single wafer for the entire family of strips, over a range of parameters. Subject to this constraint, we fixed the dimensions of the (deformable) portion of the strips to be length $L =$ 23.09 mm, width $b = 6.67$ mm, and thickness to $h = 400$ μm; see Fig. 3(a). The strip with the largest Darcy number (i.e., with the largest holes, $R_1 = 1.429$ mm), was designed to have one unit

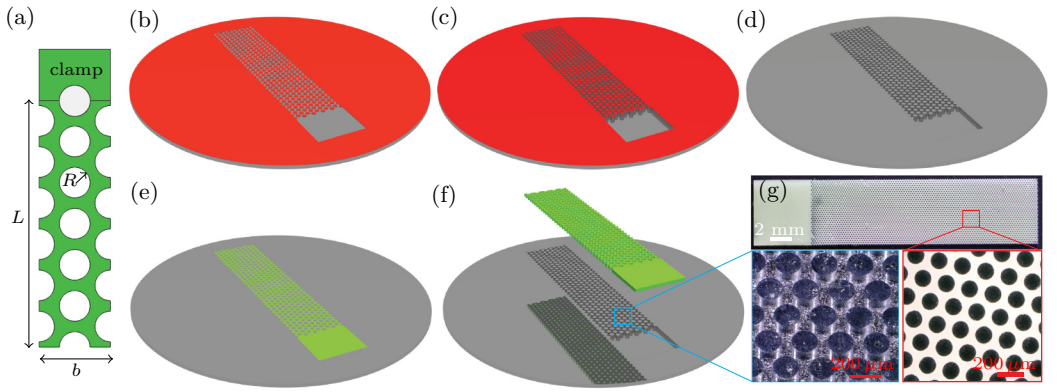

FIG. 3. (a) Representative geometry of a porous strip for $i = 1$ (i.e., $R = 1.429$ mm). The length of the strip that undergoes deformation is L and an additional length is introduced to allow for the clamping of the strip. (b)–(f) Schematic diagram of the microfabrication process. (b) Silicon wafer (gray) with a fully developed positive photoresist (red). (c) Silicon wafer after the oxide and the silicon etching processes. The desired depth due to etching sets the thickness of the strip at the end of the fabrication process. The etching depth is dictated by the buried oxide layer, which acts a stopping layer. (d) Etched wafer after removal of the photoresist, smoothing of the lateral surfaces, and conformal parylene coating. (e) Cast silicone elastomer (green) inside the mold. (f) Successful demolding of the porous elastomeric strip after swelling using isopropyl alcohol. (g) Photograph of a porous strip with $i = 16$ (top), with detailed views of the silicone mold (bottom left) and the resulting holes (bottom right).

cell along its width and three unit cells along its length. Given that the length to width ratio of the unit cell in a hexagonal lattice is $2\sqrt{3}/3$, the ratio between the length and the width of a strip was $2\sqrt{3}$. The designs of the other strips (with smaller holes) were set by increasing the number of unit cells along the width, and increasing the number of unit cells along the length, accordingly, to preserve their ratio of 3. Considering these design constraints, the layout on the 100 mm silicon wafer was set to include 13 molds for specimens, with the radii of the holes following the rule $R_i = R_1/i$, where $R_1 = 1.429$ mm and $i = \{1, 2, 3, 4, 5, 6, 8, 11, 16, 24, 32, 64, 128\}$. As such, the smallest and largest hole sizes considered were $R_{128} = 11.2$ μm and $R_1 = 1.429$ mm, respectively.

In Figs. 3(b) to 3(f), we provide a schematic diagram of the process flow that we used in the microfabrication cleanroom facilities of the Center of MicroNanoTechnology (CMi) at the École polytechnique fédérale de Lausanne. For clarity of the schematics, we depict only a single mold on the wafer, whereas, as stated above, our design comprised 13 such molds per wafer (each with different values of R). To start, we used a silicon wafer (SOI-400-3-100) that has a working area of diameter 100 mm and contains a buried layer of oxide. Through its thickness (from top to bottom), this wafer presents the following layered components: a 5 μm oxide layer, a 400 μm working silicon layer, a 3 μm buried oxide layer, and a 100 μm support silicon layer.

The microfabrication protocol that we have developed to produce our porous strips is summarized as follows:

(i) *Coating, exposure, and development of the photoresist.* As the first step in the fabrication process, we spin coated a 15 μm layer of positive photoresist AZ40XT onto the wafer. This photoresist layer was then exposed to a 405 nm laser to imprint our design of the molds, and, upon development, yielded the shape depicted in red in Fig. 3(b). The red regions in this schematic represent the portion of the wafer that is protected by the photoresist.

(ii) *Dry silicon oxide and silicon etching.* Subsequently, we performed dry etching to remove the oxide layer, and then utilized a Bosch process (for 2 h) to etch the silicon layer all the way down to the buried oxide (stopping) layer. The holes in the strip result from the negative of the pillars obtained during the etching process. Even though the Bosch process is optimized to realize pillars

that have a cylindrical geometry, they end up being slightly tapered, with a cone semiangle that remains small, not exceeding 2°. A schematic of the final output from this step is shown in Fig. 3(c).

(iii) *Conformal parylene coating.* The next step consisted in getting the mold ready for casting, including cleaning of the wafer and smoothing of the surface to ease demolding. Therefore, we removed the excess photoresist in an oxygen plasma cleaner, and then treated the silicon molds to ease the demolding process. For this purpose, we performed two different steps. First, we smoothed the vertical surfaces of the wafer, which became rough as a result of the Bosch process, by chemically forming a 2-μm-thick oxide layer, which we then removed via a chemical etching process (BHF). Then, we deposited a 200-nm-thick conformal parylene coating (after activation of the surface with Silane A174). The latter is an organic polymer that eased the demolding of silicone-based elastomers. At the end of this step, the wafer was ready for casting, as depicted in Fig. 3(d).

(iv) *Casting and demolding of the porous strips.* First, a silicone-based elastomeric solution (VPS 32, Zhermack, Italy) was poured into the molds [Fig. 3(e)] and the excess polymer was scraped off. Upon curing of the polymer (within 20 min), the specimens were retrieved from the mold. To do so, we first sprayed isopropyl alcohol on the mold, which swelled the polymer, allowing for an easier demolding and a complete removal of any remaining layer of polymer within the holes. This step ensured that the holes would be fully opened, rather than sealed by a thin elastomeric membrane. Finally, we carefully demolded the strip, as shown in Fig. 3(f).

Despite our experimental diligence, ultimately, we were able to only successfully demold nine out of the original 13 designs. The main reason for this difficulty was that the elastomer could fracture easily during demolding, especially when the radii of the holes were smaller than approximately 50 μm. In Fig. 3(g), top, we present a representative photograph for a sample ($R_{16} = 89\,\mu$m) that was successfully fabricated using the procedure detailed above. Upon demolding these samples were imaged for quality control using a digital microscope (Keyence VHR-5000), to ensure that all the holes were fully open (instead of covered by an undesirable thin polymer film). Zoomed in pictures of a representative strip and mold are shown in Fig. 3(g), bottom right and bottom left, respectively.

D. Characterization of bending stiffness of the perforated strips

Next, we performed a series of mechanical tests of the perforated strips fabricated following the protocol described in the previous section. The goal of this mechanical characterization was to quantify the bending stiffness of the specimens, knowledge of which was necessary for the analysis of the data acquired from the towing experiments. To do so, we considered a porous strip immersed in silicone oil (Bluesil 47V1000), deformed by its buoyancy-corrected weight in a cantilever configuration. We denote the density of the elastomer as $\rho = 1460\ \mathrm{kg/m^3}$, so that the apparent density will be $\Delta\rho = \rho - \rho_\mathrm{f}$, with $\rho_\mathrm{f} = \rho_\mathrm{b} = 970\ \mathrm{kg/m^3}$ for Bluesil 47V1000, as detailed in Appendix A.

We model the porous strip as an elastica, hence, obeying to the following dimensionless equation for the balance of moments [33]

$$\theta''(s) - \left(\frac{L}{L_\mathrm{eg}}\right)^3 (1-s)\cos\theta(s) = 0, \tag{6}$$

where the first term represents spatial variations of the internal moments and the second represents the moment induced by the self-weight in the cantilever configuration. As a result of the nondimensionalization, Eq. (6) involves the elasto-gravity length, defined as $L_\mathrm{eg} = \{B/[\Delta\rho g h b(1-\phi)]\}^{1/3}$. We place each of the nine strips in cantilever configuration inside the silicone oil bath and image their deformed shape at equilibrium. Notice that the elastomer swells in silicone oil, and that the degree of swelling has to be measured and taken into account in the modeling as documented in Appendix B. We then solve Eq. (6) to find the value of bending stiffness that provides the best fit of the experimental shapes, in a least-squares sense.

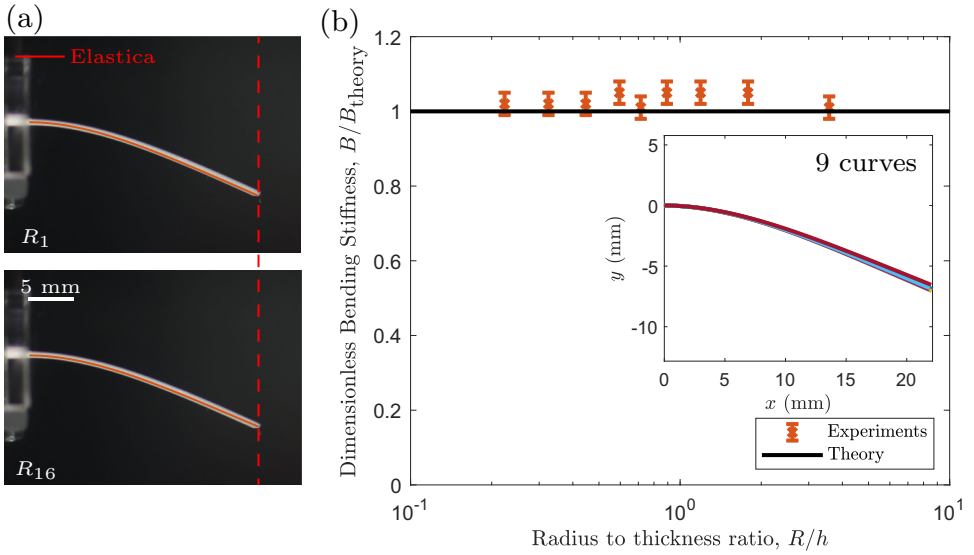

FIG. 4. (a) Comparison between experimental shapes and elastica for strips with R_1 and R_{16}. (b) Ratio between experimental and theoretical bending stiffness as a function of the ratio between the radii of the holes and the thickness of the strip. Throughout, the porosity of the perforated strips is fixed at $\phi = 0.5$. The experimental results for the nine strips (red crosses) are described, quantitatively, by the elastic model in Eq. (6) represented by the solid black line. Error bars represent uncertainties in the measurement of the length of the strip. The inset shows the experimental profiles of the nine strips under self-weight (different colored lines), whose near-perfect collapse indicates that their deformed profiles are almost identical to one another.

To verify our experimental results, we use existing results from homogenization theory [34], through which platelike porous bodies are represented by an equivalent nonporous counterpart with effective material properties that result in an effective bending stiffness,

$$B = \frac{1-\phi}{1-2\phi(\nu^2-1)} B_c, \tag{7}$$

where $\nu = 1/2$ is the Poisson's ratio of the elastomer, and the bending stiffness of the equivalent nonporous strip is $B_c = (1/12)Ebh^3$. This homogenization result holds formally as long as the characteristic length of the microstructure (R) is smaller than the thickness of the strip (h).

The results for the characterization of the bending stiffness of our porous strips are presented in Fig. 4. In Fig. 4(a), we present comparisons between elastica and experiments for strips with R_1 and R_{16}, as a result of the fitting procedure to determine the experimental value of B. In Fig. 4(b), we show the ratio between the bending stiffness that we have measured experimentally and the theoretical prediction in Eq. (7) with $\phi = 0.5$, as a function of R/h. The experimental results for the microfabricated strips are in good agreement with the theory, which does not include any variation with R/h. The inset shows the experimental profiles of the nine strips, which overlap nearly perfectly onto one another. Surprisingly, this collapse, together with the excellent agreement between experiments and theory in Fig. 4(a), suggests that the homogenization description in Eq. (7) works across the full range $R/h \in (0.2, 4)$ explored, outside of the region of formal validity of the theory ($R/h \ll 1$). These findings raise an interesting new question on the homogenization description of perforated plates, which goes beyond the scope of the current fluid-structure interaction study, but that we are planning to investigate in future work.

On a related note, the consistent agreement between the bending stiffness measurements and the effective homogenization theory results also points to the good quality of our microfabricated strips, and the invariance of the bending stiffness with the radius to thickness ratio. What this implies in

the towing experiments, then, is that if two strips deform differently for the same value of Cauchy number, then we can be confident that this difference can be directly attributed to differences in their interaction with the fluid, since they have the same bending stiffness.

III. ELASTICA-BASED MODEL FOR THE STRIPS UNDER FLUID LOADING

Having characterized the bending stiffness of the porous strips in the previous section, we now proceed by developing a theoretical description that includes the coupling between the fluid and the elastic deformation of the strip during towing. To do so, we model the strip following the classic Kirchhoff-Euler beam framework. The porous strip is modeled as an inextensible elastic beam coupled with a distributed loading that accounts for the interaction between the flexible body and the surrounding fluid, at different Reynolds numbers. As shown schematically in Fig. 2(b), the dimensionless equilibrium equations of the system can be written as [33]

$$\frac{B}{L^2}\theta''(s) + \mathbf{n}\cdot\mathbf{f} - (1-\phi)\Delta\rho g b h L(1-s)\sin\theta(s) = 0, \tag{8a}$$

$$\mathbf{f}'(s) + L\mathbf{p} = \mathbf{0}, \tag{8b}$$

where $s \in [0, 1]$ is the dimensionless arc length coordinate ($s = 1$ corresponds to the tip of the strip), θ is the angle between the tangent vector of the centerline and the vertical ($-\mathbf{e}_z$ direction), B is the bending stiffness of the strip, h is its thickness, b is its width, and $\mathbf{f}$ is the internal force, and $\mathbf{p}$ (not to be confused with the pressure field) is the fluid loading. Equation (8a) represents the local equilibrium of moments where internal moments balance those induced by the internal force $\mathbf{f}$ and the self-weight. Equation (8b) represents the local force balance. Notice that Eq. (8a) turns into the equilibrium equation of the strip under self-weight, that is, Eq. (6), if we set $\mathbf{p} = \mathbf{0}$ and $\theta(s) \mapsto \pi/2 - \theta(s)$, to rotate the configuration by 90°.

Following a similar approach to the analysis in Ref. [29], we model the strip as a homogeneous body whose density per unit homogenized volume is $(1-\phi)\rho$, where ρ is the volumetric density of the material and ϕ is the void fraction (set to $\phi = 0.5$ throughout this study). When the strip is immersed in a fluid of density ρ_f, the apparent density is $(1-\phi)\Delta\rho = (1-\phi)(\rho - \rho_f)$. We assume that the distributed fluid loading, $\mathbf{p}$, takes on different expressions relevant for low Re ($\mathrm{Re} \lesssim 1$) and moderate Re ($\mathrm{Re} \gtrsim 1$). Making use of previous work [29,35,36], we assume that the functional forms for the fluid loading in these two regimes are

$$\mathbf{p} = \begin{cases} \mathbf{p}^< = 2\frac{B}{L^3}C_Y^< c_n^< \left[\cos\theta(s)\mathbf{n} + \frac{c_t}{c_n^<}\sin\theta(s)\mathbf{t}\right] & \text{for} \quad \mathrm{Re} \lesssim 1, \\ \mathbf{p}^> = \frac{B}{L^3}C_Y^> \left[\frac{1}{2}c_n^> \cos^2\theta(s) - \frac{\pi}{4}\frac{b}{L}\theta'(s)\sin^2\theta(s)\right]\mathbf{n} & \text{for} \quad \mathrm{Re} \gtrsim 1. \end{cases} \tag{9a,9b}$$

Recall from the introduction that the Cauchy number is a dimensionless quantity that is typically used to quantify the relative importance of fluid forces versus elastic forces. In the system of Eqs. (9), two different versions of the Cauchy numbers, $C_Y^<$ (which scales with U) and $C_Y^>$ (which scales with U^2), are employed depending on the appropriate Reynolds number regime, as defined in Eqs. (4) and (5), respectively. The first, $C_Y^<$, represents the ratio between viscous and elastic forces in the low Re regime. The second, $C_Y^>$, represents the ratio between the fluid pressure and the elastic forces in the moderate Re regime. Furthermore, it is important to highlight that the first term in Eq. (9b) is the normal drag force due to pressure differences between the two sides of the strip, whereas the second term is the drag force induced by the added mass [29,35,37]. In Eq. (9a), for the low Re regime, $\mathbf{p}$ is assumed to be linearly proportional to the velocity via two local drag coefficients, which give rise to normal and tangential components of the local drag. By contrast, in Eq. (9b), for the moderate Reynolds regime, fluid drag, which is assumed to be normal to the centerline of the strip, is taken to be proportional to the square of the velocity. As a representative illustration to aid the reader visualise the fluid loading at different regimes, in Fig. 5, we plot the fluid loading profiles, as a function of arc length, for a largely deflected shape (see inset of Fig. 5). Specifically,

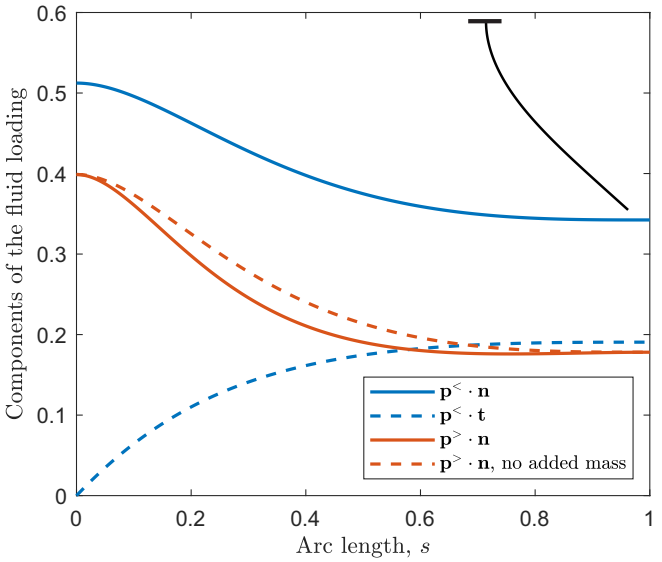

FIG. 5. Examples of fluid loading profiles, as a function of the arc length, at low Reynolds ($\mathbf{p}^<$, Re $= 0$) and moderate Reynolds ($\mathbf{p}^>$, Re $= 400$), for a representative shape of the porous strip depicted in the inset. Since the load is both tangential and normal at low Re, both projected components $\mathbf{p}^< \cdot \mathbf{t}$ and $\mathbf{p}^< \cdot \mathbf{n}$ are plotted. For the case at moderate Re, the fluid loading is plotted with and without the added mass contribution. The latter appears to be negligible even for this relatively large deflected shape.

for the case at low Re, both projected components $\mathbf{p}^< \cdot \mathbf{t}$ and $\mathbf{p}^< \cdot \mathbf{n}$ of the fluid loading are plotted (blue dashed and solid lines, respectively). These data show that the normal loading prevails over the tangential component, even in this case of large deflection. At moderate Re, the fluid loading is plotted with and without the added mass contribution (red solid and dashed lines, respectively). The added mass contribution appears to be negligible even for this largely deflected shape.

The equilibrium equation for our fluid-loaded porous strips in the system of Eqs. (8), with the appropriate fluid loading depending on the range of Reynolds numbers as set by Eqs. (9), is completed with the appropriate boundary conditions. At the clamped end, we have $\theta(s = 0) = 0$. At the free end ($s = 1$), since there are no applied moments, we should impose a zero-curvature condition, $\theta'(1) = 0$. However, the fabricated samples could present a small intrinsic (natural) curvature due to slight asymmetric conditions during the curing of the elastomer in their molds. Still, even if this natural curvature κ_0 is unavoidable due to experimental artifacts, it can be measured *a posteriori* with the strip at rest (no fluid loading) and modeled as an applied moment at the free end as $\theta'(1) = L\kappa_0$ [33]. Had the natural curvature been not homogeneous, the modeling would have required a modification of the bulk equation. Combining the system of Eqs. (8), and imposing that no force is applied at the free end, $\mathbf{f}(1) = \mathbf{0}$, we get for low Re number regime

$$\theta''(s) + 2C_Y^< c_n^< \mathbf{n} \cdot \int_1^s \left[\cos\theta(s)\mathbf{n} + \frac{c_t}{c_n^<}\sin\theta(s)\mathbf{t}\right] ds - \left(\frac{L}{L_{eg}}\right)^3 (1-s)\sin\theta(s) = 0, \tag{10}$$

and for moderate Re number regime

$$\theta''(s) + C_Y^> c_n^> \mathbf{n} \cdot \int_1^s \left[\cos^2\theta(s) - \frac{\pi}{4}\frac{b}{L}\theta'(s)\sin^2\theta(s)\right]\mathbf{n}\, ds - \left(\frac{L}{L_{eg}}\right)^3 (1-s)\sin\theta(s) = 0. \tag{11}$$

Equations (10) and (11) highlight three different dimensionless quantities that we regard as the primary parameters in our problem: the so-called rescaled Cauchy number $C_Y^< c_n^<$ or $C_Y^> c_n^>$ [32], the

ratio between the tangential and normal drag coefficients (for low Re flows) $c_t/c_n^<$, and the ratio between the length of the strip and the elasto-gravity length.

Numerical solutions for Eqs. (10) and (11), which are integro-differential equations, under the appropriate boundary conditions are obtained using finite-difference method, as done in Ref. [29]. The local deflection is initiated with a small disturbance and then updated over iteration until convergence. The code is implemented in Python and can be used in two different ways depending on whether the local drag coefficients are known or not. As we will show in Sec. V A, since the deformations considered in this study are such that the angle at the tip does not exceed 45°, the deformed shape of the elastica is nearly insensitive to $c_t/c_n^<$, making it difficult for the least-squares optimization to provide a satisfactory numerical estimate of this ratio. Consequently, since the value of the tangential drag coefficient will not affect the least-squares optimization, we assume $c_t/c_n^< = 1/2$, consistently with slender body theory [37]. Had the deformation of the strips been larger, the elastica model would have been unsuited since the strip would have experienced a non-negligible axial load.

In the next Sec. IV, we will show that for low Re flows, we can estimate the local drag coefficient from the Stokes simulations of a rigid strip in perpendicular flow conditions. Then, in Sec. V A, we will use these results for rigid strips combined with Eq. (10) to obtain predictions in the low Re number regime for the deformed shape that are in good agreement with experiments. For moderate Re numbers, in Sec. V B we will use Eq. (11) to estimate the local drag coefficient by fitting the predicted shape to the experimental shape via least-squares optimization.

IV. NUMERICAL SIMULATIONS OF RIGID POROUS STRIPS IN THE LOW RE REGIME

In this section, we describe the computational framework that we have employed to perform numerical simulations for the specific case of creeping flow regime (i.e., in the low Re regime described by Stokes equations) with *rigid* (not flexible) porous strips. This regime is represented by the circles in the (Re, C_Y) parameter space shown in Fig. 2(c) The ultimate goal of this computational effort is to, eventually (in Sec. V), be able to obtain predictions for the deformed profile of the more general case of flexible strips. The rigid strip is clamped perpendicularly to the horizontal free surface of the bath of the viscous fluid. Furthermore, we assume that (a) the root of the strip is located at the same height of the free surface and (b) the flow is perpendicular to the strip. These conditions correspond to a largely simplified and limiting case of the experimental scenario. For the simulations in this section, the porous strips are assumed to have infinite bending stiffness, $B = \infty$, such that the Cauchy number is $C_Y^< = 0$ and the elasto-gravity length is $L_{eg} = \infty$. We will follow three steps:

(1) First, we will compute the drag coefficient for a *rigid* strip from the numerical simulations of the Stokes equations described below, as discussed in detail in the present section.

(2) Secondly, we will insert this drag coefficient for a rigid strip into the *elastica* description for *flexible* strips; i.e., the equation of equilibrium presented above in Eq. (10). In doing so, we will implicitly assume that the local drag coefficient of the rigid strip under perpendicular flow condition can be taken as the local drag coefficient of the corresponding deformable strip, similarly to Ref. [32].

(3) Finally, the obtained predictions for the deformed shapes will be contrasted against the experimentally obtained strip profiles.

For now, let us turn our attention to the special case of a rigid strip under low Re number conditions. It is well established that low Re flows can described by the incompressible Stokes equations [36]:

$$\begin{aligned} \nabla p &= \mu \nabla^2 \mathbf{u}, \\ \nabla \cdot \mathbf{u} &= 0, \end{aligned} \tag{12}$$

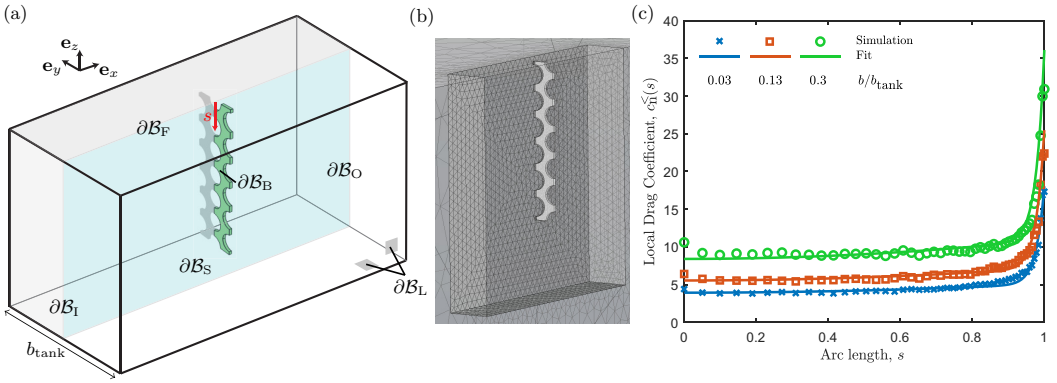

FIG. 6. (a) Schematic diagram (not to scale) of the geometry of the numerical simulations solving the Stokes equations for the flow past a *rigid* porous strip. The porous strip is placed vertically in the middle of the fluid tank, with the clamped end at the same height of the free surface $\partial\mathcal{B}_\mathrm{f}$. The symmetry plane cuts the domain and the strip into two halves, resulting in the creation of the surface $\partial\mathcal{B}_\mathrm{S}$. (b) Example of a meshed geometry used in the simulations, showing the refinement region in the neighborhood of the body. (c) Local drag coefficient as a function of the arc length s, for different confinement ratios b/b_tank. The data points represent the results obtained from the Stokes simulations, whereas solid lines represent the proposed fit [Eq. (16)]. In these three simulations, $\mathrm{Re} = 0$ since we solve the Stokes equations, and $R/h = 3.6$ and $h/L = 0.017$.

where p denotes the pressure field and $\mathbf{u}$ is the velocity vector field. We assume these equations to be valid throughout the control volume coinciding with the tank used in the experiments. As sketched in Fig. 6(a), the flow is described in a Cartesian coordinate system fixed to the strips, with the x direction aligned with the incoming relative flow velocity, $\boldsymbol{u}$. We complete the Stokes equations with the following boundary conditions. At the inlet and lateral boundaries, $\partial\mathcal{B}_\mathrm{I}$ and $\partial\mathcal{B}_\mathrm{L}$, respectively, we assign a uniform velocity, $\mathbf{u} = U_\infty \mathbf{e}_x$. A homogeneous Dirichlet condition is considered on the surface of the strip $\partial\mathcal{B}_\mathrm{B}$ (i.e., $\mathbf{u} = \mathbf{0}$). Moreover, no-stress conditions are applied to both the outlet boundary $\partial\mathcal{B}_\mathrm{O}$ and the free-surface $\partial\mathcal{B}_\mathrm{F}$, which we also assume to be flat $\mathbf{u} \cdot \mathbf{e}_z = 0$. Symmetry along the midplane $\mathcal{B}_\mathrm{S}$ was imposed by requiring $\mathbf{u} \cdot \mathbf{e}_y = 0$ and a zero tangential stress.

The system of Eqs. (12) can be recast in weak form:

$$\int (\mu \boldsymbol{\nabla}\mathbf{u} \cdot \boldsymbol{\nabla}\tilde{\mathbf{u}} - p\boldsymbol{\nabla} \cdot \tilde{\mathbf{u}})\, dV = 0, \quad \forall \tilde{\mathbf{u}},$$
$$\int \tilde{p}\boldsymbol{\nabla} \cdot \mathbf{u}\, dV = 0, \quad \forall \tilde{p}, \tag{13}$$

where the test functions are denoted by $\tilde{\mathbf{u}}$ and $\tilde{p}$. We used quadratic Lagrangian shape functions for the velocity field, and Lagrangian linear shape functions for the pressure field. The system of Eqs. (13) was implemented in COMSOL Multiphysics (COMSOL, v.5.2) using the partial differential equations (PDEs) Weak Form node. An internal subregion was created to control the mesh density, which was specified by the vertex densities imposed on the corresponding edges. The typical number of degrees of freedom was approximately 3×10^6, a value that was set after a convergence study. A representative example of the meshed geometry employed in the simulations is presented in Fig. 6(b). Given that low Re flows are known to be sensitive to wall effects, we performed a systematic parametric investigation of the width of the fluid domain in a way that encompassed the dimensions of the experimental tank. A typical simulation run for a fixed set of parameters on a workstation with 12 cores at 3.0 GHz and 128 GB of RAM took approximately 15 min.

From the simulations described above, we computed the local drag coefficient $c_n^<(s)$, which depends on the arc length, s, along the strip, as

$$c_n^<(s) = \frac{2}{\mu U}\int\left\{pn_x - \mu\left[2\frac{\partial u_1}{\partial x}n_x + \left(\frac{\partial u_1}{\partial y} + \frac{\partial u_2}{\partial x}\right)n_y + \left(\frac{\partial u_1}{\partial z} + \frac{\partial u_3}{\partial x}\right)n_z\right]\right\}dC, \tag{14}$$

where $n_x = \mathbf{n}\cdot\mathbf{e}_x$, with $\mathbf{n}$ as the unit vector normal to one of the surfaces of the body, $\mathbf{u} = u_1\mathbf{e}_x + u_2\mathbf{e}_y + u_3\mathbf{e}_z$, and C represents the boundary curve of the cross section of the strip located at s. The prefactor of 2 in Eq. (14) results from the fact that the integration is performed over half of the body by taking symmetry into account.

In Fig. 6(c), as an illustrative example of the type and quality of the numerical results that we can compute, we present a subset of data for the local drag coefficient, $c_n^<$, as a function of the arc length, s, for three different values of the aspect ratio between the widths of the tank and the strip. These data indicate that the local drag coefficient is approximately constant across most of the arc length of the strip, except for a small region near the tip where it increases sharply by up to a factor of 5. Given that, in the deformable case relevant to the experiments, the porous strip will deform in bending, this region of local viscous forces near the tip cannot be neglected. Consequently, in the elastica model introduced in Eqs. (10), we consider the following functional form for the local drag coefficient for Stokes flows

$$c_n^<(s) = \overline{c}_n^<\gamma(s), \tag{15}$$

where $\overline{c}_n^<$ is the average drag coefficient along s that depends on the experimental conditions (e.g., b/b_{tank}, R/h, h/L, b/L, and ϕ) and $\gamma(s)$ is a shape function describing how the local drag coefficient (i.e., the local fluid forces), varies along the arc length of the strip. Inspired by the results in Fig. 6(c), we have chosen the following empirical representation of the shape function

$$\gamma(s) = 1 + \frac{\alpha}{\beta}\log(1-\beta) + \frac{\alpha}{1-\beta s}, \tag{16}$$

where the second term has been determined such that the function has a normalized average value of $\langle\gamma(s)\rangle = \int_0^1 \gamma(s)\,ds = 1$. For the values of h/L, b/L, and ϕ characterizing our experiments, the fitting parameters have been determined to be $\alpha = 0.022 \pm 0.002$ and $\beta = 0.991 \pm 0.001$ for the different values of b/b_{tank} that we explored. Note that, having determined the values of α and β, once and for all, the only free fitting parameter is the average drag coefficient $\overline{c}_n^<$. As shown in Fig. 6(c), Eq. (15), with $\gamma(s)$ given by Eq. (16), is found to be a satisfactory empirical description (solid lines) of the numerical results for $c_n^<(s)$, for different values of b/b_{tank}.

V. RESULTS

Thus far, we have defined our problem, introduced the experimental protocol (including the characterization of the bending stiffness of the strips), and described our modeling approach. We now proceed by reporting our experimental results on the towing experiments, contrasting them with numerical simulations wherever possible. We will first present results at creeping flow conditions, with a focus on the tip displacement of the strips and the quantification of the corresponding drag coefficients during towing. Afterwards, given that bodies at low Reynolds numbers experience drag forces that are sensitive to their proximity to the boundaries (i.e., walls or the free surface), we will characterize the so-called *wall effect* for the geometries considered in the current study. Here, we will follow an approach similar to that used for the investigation in Ref. [26], for rigid porous disks driven through a viscous fluid. We will then turn to the case of moderate Reynolds numbers and seek to quantify the dependence of the drag coefficients as a function of permeability (i.e., Darcy number). Finally, we will study the reconfiguration of porous strips in the various regimes of Reynolds number explored. In this way, we will provide a quantitative characterization of the drag coefficient of flexible porous strips with different values of the permeability, from low to moderate Reynolds numbers.

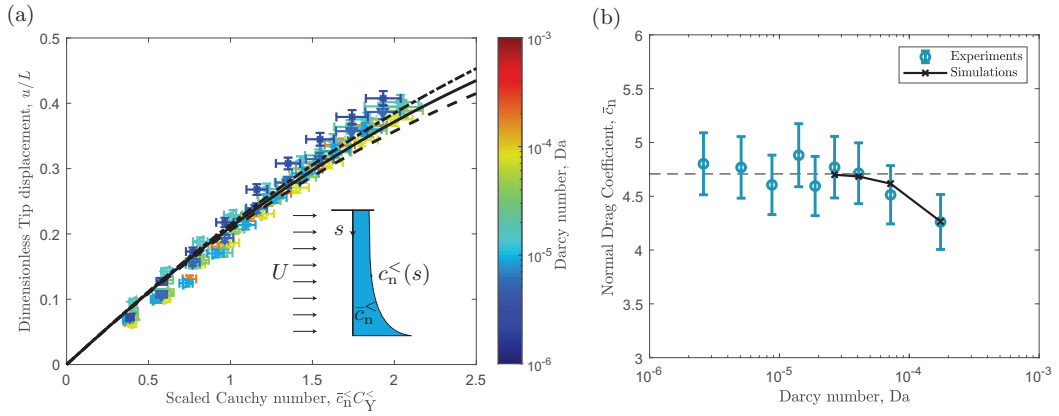

FIG. 7. (a) Dimensionless tip displacement u/L versus the scaled Cauchy number $\bar{c}_n^< C_Y^<$, for the nine porous strips. The elastica model with the normal drag coefficients determined via Stokes simulations on rigid strip agrees well with experiments. The solid line represents the solution for $c_t/\bar{c}_n^< = 1/2$, the dashed line corresponds to $c_t/\bar{c}_n^< = 0$, whereas the dashed-dotted line represents the case $c_t/\bar{c}_n^< = 1$. The color bar indicates the Darcy number. Error bars on the tip displacement correspond to the standard deviations of the 10 measurements for each case, whereas error bars on the x axis are the results of uncertainties in the Cauchy number, via the bending stiffness. (b) Normal drag coefficient as a function of Darcy number: experiments (blue circles) are well described by Stokes simulations on rigid strips (black crosses for the first four strips with the largest radii, and dashed line for the impermeable strip). Error bars correspond to the standard deviations of the 10 independent but otherwise identical measurements, performed at each value of Da.

A. Towing porous strips at low Re number conditions

We start by focusing on the deformation of porous strips, which we quantify via their tip displacement, for different values of the Cauchy number $C_Y^< \in [0.05, 0.5]$, in the creeping flow regime [circles in the $(\mathrm{Re}, \mathrm{C_Y})$ parameter space shown in Fig. 2(c)]. In Fig. 7(a) we plot the magnitude of the displacement vector of the tip (with respect to its planar, undeformed configuration) normalized by the strip length L, that is u/L, as a function of the scaled Cauchy number $\bar{c}_n^< C_Y^<$ defined in Sec. III. Here the normal drag coefficients was determined in advance, using the Stokes simulations described in Sec. IV. As mentioned in Sec. III, the ratio $c_t/\bar{c}_n^<$ does not influence significantly the deformation of the strip. In Fig. 7(a) we substantiate this statement by contrasting the experimental data for u/L against the elastica solutions obtained by solving Eq. (10) using either of the following three assumptions: (a) $c_t/\bar{c}_n^< = 1/2$ (solid black line); (b) $c_t/\bar{c}_n^< = 0$ (dashed line); or $c_t/\bar{c}_n^< = 1$ (dashed-dotted line). We find that the experimental results for strips with different hole sizes (i.e., different values of the Darcy numbers, Da) show a good collapse, which is in good agreement with the elastica model at low Reynolds, Eq. (10), using the normal drag coefficients determined via Stokes simulations. Furthermore, the numerical results (solid, dashed and dashed-dotted lines, corresponding to the above three assumptions) show that the details of the ratio of the drag coefficients, $c_t/\bar{c}_n^<$, do not influence the results significantly, especially in the regions of interest of the experimental data. For example, the relative variation of the three cases is 4% when $\bar{c}_n^< C_Y^< = 1.5$ and 5% when $\bar{c}_n^< C_Y^< = 2.5$. Finally, as discussed in Sec. III, it is important to independently measure the natural curvature of the strip and use this value as an input parameter into the numerical framework. For all of the nine porous strips tested experimentally, we measured a normalized curvature of $\kappa_0 L = 0.15 \pm 0.03$, independently of the hole size of the specimen. Had we not done so and incorrectly assumed the natural curvature to be zero, we would have overestimated the drag coefficient by up to 31%.

In Fig. 7(b) we present the variation of the (average) normal drag coefficient, $\bar{c}_n^<$, as a function of Darcy number, Da, obtained from the experiments (fitting of the experimental shape to the shape

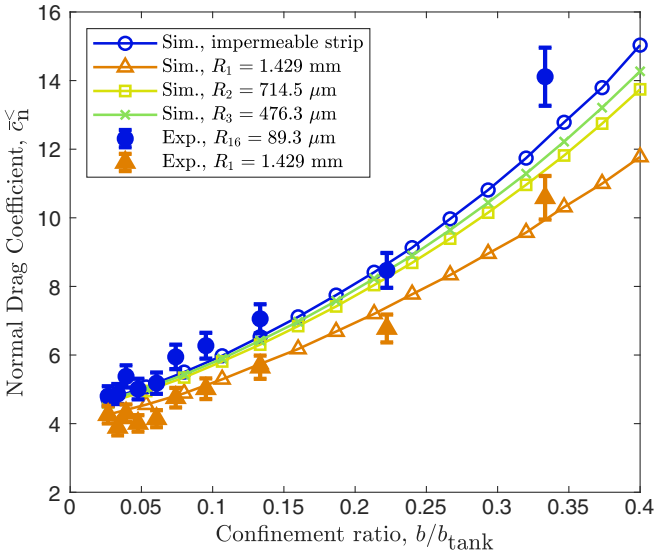

FIG. 8. Normal drag coefficient as a function of the confinement ratio b/b_{tank}. Experiments on strip with R_1 (orange closed symbols) and R_{16} (blue closed symbols) are well described by the numerical simulations (open symbols), which we performed for the first three strips with the largest radii and the impermeable strip. The error bars indicate the standard deviations of the 10 measurements that we performed for each case.

predicted by the elastica; Sec. III) and from the simulations (Stokes simulations of rigid strips in perpendicular flow conditions; Sec. IV). The numerical simulations were carried out only for the subset of four strips with the largest radii, that is, $i = \{1, 2, 3, 4\}$, since the convergence for smaller values of R required a number of degrees of freedom much larger than 3×10^6, unattainable using our computational capabilities. To address this limitation, we carried out a simulation on an impermeable strip to determine its drag coefficient, with the rationale that both experiments and simulations on porous strips approach this value as the Darcy number decreases. Practically, we find that the drag coefficient for a porous strip with $R/h \leqslant 1$ is nearly the same as the drag coefficient of an impermeable strip, which is shown as a dashed horizontal line in Fig. 7(b). For example, if we compare the drag coefficients between two strips with R_4 and R_3, we can measure a relative difference of 0.4%, and this difference only gets increasingly smaller for strips with smaller holes, becoming practically zero for radii smaller than R_4. This is consistent with findings at low Re as those reported in Refs. [18,38].

Turning now to wall effects, we performed the towing experiments for the strips with $R_1 = 1.429$ mm and $R_{16} = 89.3$ μm (i.e., the strips with the largest and smallest holes, respectively, in our set) and varied the width of the tank while fixing the width of the strips to $b = 6.67$ mm, such that the confinement ratio was explore in the range $b/b_{\text{tank}} \in [0.03, 0.35]$. For this experiments, we inserted two rigid acrylic walls in the tank on either side of the strip and with their length aligned along $\mathbf{e}_x$, and systematically approached them along the width ($\mathbf{e}_y$). In parallel, we also performed Stokes simulations by parametrically varying the width of the fluid tank. As the memory requirements become impractical for strips with $i \geqslant 4$, we will compare the experimental results for $R_{16} = 89.3$ μm with the numerical simulations on an impermeable strip. This approximation is justified given that the drag coefficients of strips with $i \geqslant 4$ are nearly identical to the one of the impermeable strip, as evidenced above in Fig. 7(b) via the numerical results.

The results for this investigation on wall effects are summarized in Fig. 8, where we plot the normal drag coefficient as a function of the confinement ratio. We find that the experimental results agree well with the numerical simulations, where the drag coefficient increases up to about 3 times

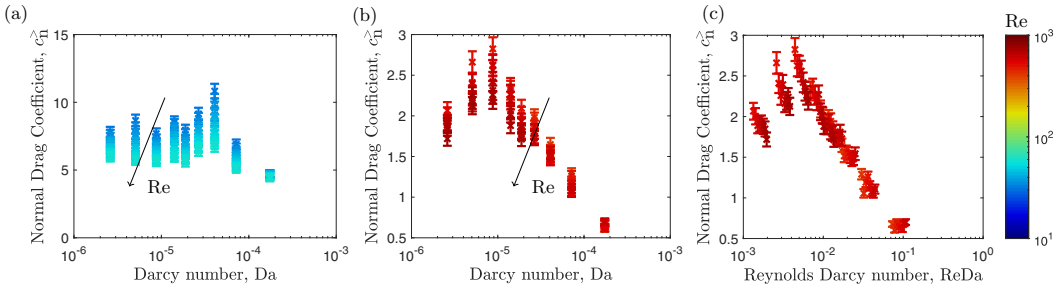

FIG. 9. Drag coefficient at moderate Reynolds numbers. (a) The nonmonotonic behavior of the normal drag coefficient as a function of the Darcy number for $\mathrm{Re} \in (10, 60)$. (b) Normal drag coefficient versus Darcy number for $\mathrm{Re} \in (400, 800)$. (c) Normal drag coefficient as a function of the product between Darcy and Reynolds numbers for $\mathrm{Re} \in (400, 800)$. The color bar indicates Reynolds numbers. Error bars in each of the three plots correspond to the standard deviations of the 10 independent but otherwise identical measurements, performed at each value of Da.

for a confinement ratio that increases from 0.03 to 0.3. As it was also observed in a previous study [26] for rigid porous disks with fixed porosity and varying permeability, the wall effect strongly depends on the Darcy number. In particular, we find that the curves for the drag coefficient spread further apart from one another as the confinement ratio increases, meaning that the effect of permeability on the wall effect increases as confinement increases. This has to be carefully taken into account whenever one performs an experiment in a confined environment to estimate the drag coefficient of the sample in an infinite bath.

B. Moderate Reynolds numbers

We now turn our attention to the case of moderate Reynolds numbers, to study the effect of fluid inertia on both the deformation of the porous flexible strips and the associated drag coefficients. To have access to the ranges $\mathrm{Re} \in (10, 60)$ and $\mathrm{Re} \in (400, 800)$, we used different fluids, as mentioned in Sec. II, and whose characterizations are provided in Appendix A. These two regimes are represented by the crosses and the triangles, respectively, in the $(\mathrm{Re}, \mathrm{C_Y})$ parameter space shown in Fig. 2(c). In these ranges, the strip exhibits small oscillations at equilibrium (vortex-induced vibration), so that the extracted experimental shape of the strip is the result of a time average of the shapes over two periods of oscillations at steady state (Sec. II). The experimental results from these experiments are represented in Fig. 9.

In Fig. 9(a) we plot the normal drag coefficient versus the Darcy number for $\mathrm{Re} \in (10, 60)$. Differently from creeping flow conditions, the drag coefficient varies nonmonotonically with the Darcy number, exhibiting a maximum for $\mathrm{Da} \simeq 5 \times 10^{-5}$, which corresponds to $R/h \simeq 1$. It is also apparent from these data that, for a a given porous strip (i.e., fixed value of Darcy number), the drag coefficient decreases with Re (represented in the color bar to the plot). The results for higher values of the Reynolds numbers, $\mathrm{Re} \in (400, 800)$, are plotted in Figs. 9(b) and 9(c). The former describes the behavior of the $c_n^>$ as a function of the Da, showing again a nonmonotonic behavior, with a maximum now around $\mathrm{Da} \simeq 5 \times 10^{-6}$, which corresponds to $R/h \simeq 0.3$. In Fig. 9(c) we plot the same data as in Fig. 9(b), but rescaling the x axis as the product of the Darcy and Reynolds numbers, ReDa. This choice is motivated by a previous study in the high permeable regime ($\mathrm{Da} \to 1$), which suggested that the drag coefficient is a function of ReDa [19,21]. Indeed, even though this rescaling of the x axis should cause a collapse of the data only for $\mathrm{Da} \to 1$, Fig. 9 shows a good collapse of the data over a wider range. The error bars in the three plots correspond to the standard deviations of the 10 measurements that we performed for each case.

As deformation is directly proportional to the drag coefficient, this nonmonotonic variation of the drag coefficient translates into a nonmonotonic variation of the tip displacement of porous strips

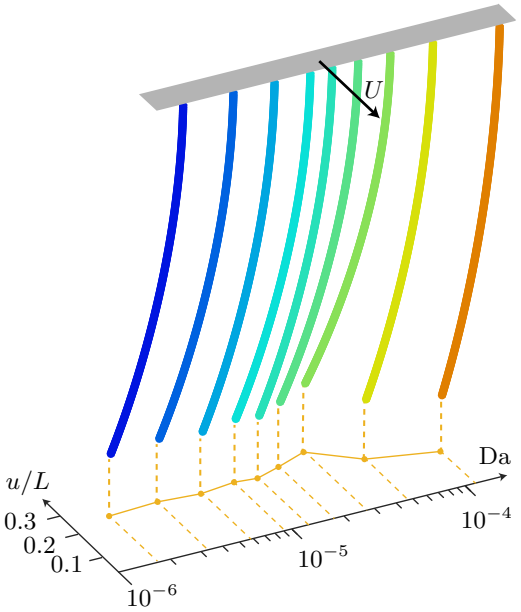

FIG. 10. Deformation of the porous strips at Re = 50, shown via the fitted shapes with the drag coefficients reported in Fig. 9(a). Since deformation is proportional to the drag coefficient, the behavior of $c_n^>$ with the Darcy number can be seen here graphically, in terms of the dimensionless tip displacement u/L, which indeed varies nonmonotonically with permeability.

as a function of the Darcy number. We show this in Fig. 10 for Re = 50, where we plot the fitted shapes with the drag coefficients that have been presented in Fig. 9(a) for different values of the Darcy number. The tip displacement is also reported in the projection in the (Da, u/L) plane, and it is shown to vary nonmonotonically with the Darcy number, similarly to the variation of the drag coefficient.

Above, we presented results in the moderate Reynolds number regime, up to Re = 800. It is of interest to compare these results with existing results on flexible porous strips at high Re, as those presented in Ref. [29] (where the lower bound was Re > 5000). In their study, in addition to focusing on higher values of Re than we do here, the authors varied porosity and permeability in a coupled way. By contrast, in the present study, we fixed the porosity of our strips and systematically varied permeability. Still, we can attempt to contrast our results above to those of Ref. [29]. Since we fixed $\phi = 50\%$ in our study, we have to restrict our comparison only to results corresponding to that specific value of ϕ from their study that has a counterpart in the value for permeability in the present study. As a result, the only comparable configuration is that corresponding to R_1. For this case, our determined drag coefficient is $c_n^> \approx 0.5$ [reported in Fig. 9(b)], which is consistent with the corresponding configuration in Ref. [29], despite their higher range of Re. However, had the authors varied permeability (independently from porosity), as we did here, they would have observed a multitude of drag coefficients in a wide range, as we found in our experiments [see Fig. 9(b)]. We hope that these results will motivate future studies at high Re regimes that are analogous to what we have done here—independently controlling permeability and porosity—so as to decouple the two effects.

C. Global drag: Reconfiguration of the porous strips at low to moderate Re

Having characterized the dependence of the local drag coefficient of our flexible porous strips on Re and Da, we now turn into characterizing the total (global) drag of the porous strips as a function

of Cauchy number, toward the goal of studying their reconfiguration at different flow conditions. The term reconfiguration is usually employed to describe the drag reduction induced by the deformation of the structure, which tends to align itself with the flow (the act of streamlining) [9]. We will start by defining the reconfiguration number [39] and then evaluate it in the two different cases of low and moderate Reynolds numbers.

The reconfiguration number $\mathcal{R}$ is defined as the ratio between the total drag force D on a deforming structure and the total drag force on the equivalent rigid one, $\theta(s) = 0$, that is,

$$\mathcal{R} = \frac{D}{D|_{\theta=0}}, \tag{17}$$

where the drag is evaluated in the direction of towing; $D = \mathbf{f} \cdot \mathbf{e}_x$. To distinguish between drag forces at low and moderate Reynolds numbers, we introduce the symbols $D^<$ and $D^>$, respectively, which correspond to integrating the fluid forces at low Reynolds, $\mathbf{p}^<$, and moderate Reynolds, $\mathbf{p}^>$, defined in Eq. (9), to obtain $\mathbf{f}^<$ and $\mathbf{f}^>$ via Eq. (8b).

A detailed investigation of the reconfiguration of nonporous strips at moderate Reynolds numbers has been performed in Ref. [32], where a model was proposed comprising a local drag coefficient, which was independent of reconfiguration and equal to the drag coefficient of the rigid strip in perpendicular flow. In this way, the total drag force could be easily computed as a function of the local drag coefficient and the deformed shape of the strip, $\theta(s)$, as

$$D^> = \mathbf{f}^> \cdot \mathbf{e}_x = \frac{1}{2}\rho_\mathrm{f} U^2 b L c_\mathrm{n}^> \int_0^1 \cos^3\theta(s)\, ds, \tag{18}$$

where $c_\mathrm{n}^>$ can be pulled out of the integral since it is assumed to be homogeneous. Furthermore, we have neglected the added mass contribution since it is two orders of magnitude smaller than the pressure term. This can be understood by noting that the deformations in the moderate Re experiments are small ($\theta(s) < \pi/6$), leading to $\theta'(s)\sin^2\theta(s) \ll \cos^2\theta(s)$. Since the rigid strip case implies that $\theta(s) = 0$, the corresponding total drag force is $D^>|_{\theta=0} = 1/2\rho_\mathrm{f} U^2 b L c_\mathrm{n}^>$. Therefore, we can compute the reconfiguration number at moderate Re numbers via Eq. (17) as

$$\mathcal{R}^> = \frac{D^>}{D^>|_{\theta=0}} = \int_0^1 \cos^3\theta\, ds. \tag{19}$$

If we apply the same arguments to our case at low Reynolds numbers, considering also that $c_\mathrm{n}^<$ is a function of the arc length, we can derive the drag force to be

$$D^< = \mathbf{f}^< \cdot \mathbf{e}_x = \bar{c}_\mathrm{n}^< \mu U L \int_0^1 f(s)\cos^2\theta\, ds + c_\mathrm{t}\mu U L \int_0^1 \sin^2\theta\, ds, \tag{20}$$

and then derive the reconfiguration number defined at low Re as

$$\mathcal{R}^< = \frac{D^<}{D^<|_{\theta=0}} = \int_0^1 f(s)\cos^2\theta\, ds + \frac{c_\mathrm{t}}{\bar{c}_\mathrm{n}^<}\int_0^1 \sin^2\theta\, ds. \tag{21}$$

In Fig. 11 we plot the reconfiguration number as a function of the scaled Cauchy number in the three different regimes of Reynolds number that we explored, namely, the low Re regime $\mathrm{Re} \in (0.001, 0.01)$, and the moderate Re regimes $\mathrm{Re} \in (10, 60)$ and $\mathrm{Re} \in (400, 800)$. In the plot, symbols represent experimental results, corresponding to the different range of Reynolds numbers. These results for $\mathcal{R}$ were obtained by invoking Eqs. (21) and (19) with the experimentally measured $\theta(s)$, and using the drag coefficients determined via the least-squares fitting procedure detailed in Sec. III, plotted in Figs. 7(b) and 9(a)–9(c). The solid blue line represents the numerical results for moderate Re number obtained by plotting Eq. (19) and the black line corresponds to the low-Re case obtained from Eq. (21), where we use the drag coefficients obtained from the fitting. While the agreement between experiments and numerics is not surprising, since the drag coefficients have been determined via least-squares fit of the elastica shape to the experimental shape, the spread of

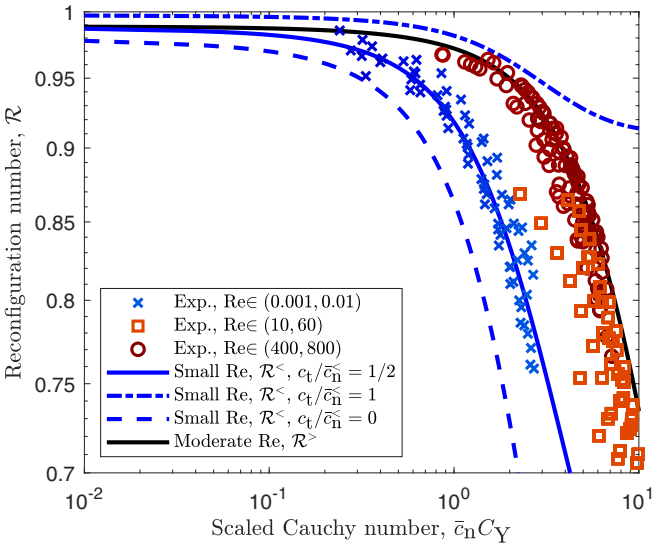

FIG. 11. Reconfiguration number versus the scaled Cauchy number for low and moderate Reynolds numbers. Symbols represent experimental results, where we use the global drag coefficients ($\bar{c}_n^<$ for low Reynolds and $c_n^>$ for moderate Re) determined via the least-squares fitting procedure described in Sec. III. The color bar indicates the Reynolds number for the experimental results. Solid lines are theoretical predictions for the reconfiguration number at low Re, $\mathcal{R}^<$, via Eq. (21) (solid blue line) and the reconfiguration number at moderate Re, $\mathcal{R}^>$, via Eq. (19) (solid black line). The dashed blue line represents the reconfiguration number for low Reynolds numbers, in the case $c_t/\bar{c}_n^< = 0$, whereas the dashed-dotted line corresponds to the case $c_t/\bar{c}_n^< = 1$.

the experimental results conveys the uncertainty of this estimation procedure. The plot shows how our porous strips undergo reconfiguration with a drag reduction up to 30%. Moreover, note that the transition between small and large reconfigurations occurs around $\bar{c}_n^< C_Y \simeq 1$.

Since the drag force is not measured independently via a load cell, as it was done for example in Ref. [32], we might, in reverse, have regarded the deformed porous strip as an indirect load cell. However, since in the low Re case we cannot determine the tangential drag coefficient via fitting as explained in Sec. V A, the lack of an independent force measurement gives rise to an indeterminacy in the evaluation of the drag force and, therefore, the reconfiguration number. Indeed, notice that the reconfiguration number for low Re plotted in Fig. 11 corresponds to $c_t/\bar{c}_n^< = 1/2$, which we assumed in our analysis. While this choice does not influence the predictions on tip displacement and normal drag coefficient as shown in Sec. V A, it has large consequences on the total drag force. In particular, the dashed line in Fig. 11 represents the reconfiguration number for $c_t/\bar{c}_n^< = 0$, which would correspond to the total absence of skin friction, whereas the dashed-dotted line corresponds to the case $c_t/\bar{c}_n^< = 1$, which would correspond to an isotropic drag. We can observe how, in the absence of skin friction, the drag ratio drops considerably more than in the case with $c_t/\bar{c}_n^< = 1$, where streamlining does not necessarily corresponds to a large drag drop.

Overall, the above results indicate that, since the reconfiguration number at low Re depends strongly on $c_t/\bar{c}_n^<$, the independent measure of the drag force via a load cell is necessary for the correct evaluation of the total drag force. As we showed in Sec. V A, other quantities such as the deformation of the strip and its normal drag coefficient are insensitive to the ratio of the drag coefficients and can be readily determined both experimentally and numerically (Stokes simulations). By contrast, at moderate Reynolds numbers, given a vanishing skin friction ($c_t \simeq 0$) in this regime, the evaluation of the normal drag coefficient via the least-squares procedure is sufficient for the quantification of the drag force.

VI. DISCUSSION AND CONCLUSION

We have investigated the interaction between porous deformable strips and viscous fluids, both at low and moderate Reynolds number regimes. Our goal was to study the drag coefficient and the deformation of the strips, while fixing their weight (i.e., porosity), and systematically varied their permeability. To do so, we microfabricated nine porous strips with fixed porosity and different permeabilities. We characterized the mechanical properties of the prototypes, finding a constant bending stiffness, which is fixed by porosity, independently of permeability. Toward understanding how these structures deform when interacting with the surrounding fluid, we performed towing experiments to determine the local drag coefficients of the strips and characterized their deformation. In parallel, we performed computer simulations where the strip was modeled as an *elastica*, with drag coefficients that were regarded as fitting parameters to model the experimental shapes.

At low Re, we found that the drag coefficient depends only slightly on permeability, varying by at most 10%, as shown in Fig. 7, and being therefore mostly determined by porosity (weight). These results are consistent with previous studies at creeping flow conditions, as shown, for example, for annuli [18] and porous disks [26]. This finding can be rationalized by the fact that, given the negligible effect of inertia at low Re, such flows are not sufficiently "energetic" to pass through (the pores of) the structure, which, therefore, behaves as an impermeable (nonporous) one. Moreover, we found that the shape of the strip can be quantitatively predicted if we feed the elastica model with the normal drag coefficient determined via Stokes simulations on a rigid strip in perpendicular configuration (similar to what has been shown in Ref. [32]).

At moderate Re, when the inertia of the flow becomes nonnegligible, either by decreasing the viscosity of the fluid or increasing the characteristic flow velocity, some portions of the flow are sufficiently "energetic" to go through the holes, provided these are not too small. In this regime [Fig. 9(a), for $\mathrm{Re} \in (10, 60)$, and Fig. 9(b), for $\mathrm{Re} \in (400, 800)$], we find that the drag coefficient depends strongly on permeability. This marked difference with respect to the low Re regime suggests that permeability plays a major role in FSI at moderate Re. We regard this difference in behavior between the low and moderate Re regimes as the primary finding of the present study, evidencing the importance of assessing the drag coefficient of porous structures at constant weight conditions. These findings fill the gap with respect to past studies where porosity and permeability were varied simultaneously.

As an illustration of the significance of the findings summarized above, let us consider, by way of example, an insect or a microdrone, whose morphology is to be optimized to maximize its drag coefficient, for a set payload (weight). At low Re, our results suggest that the morphological details do not play a primary role, as long as the porosity is fixed. By contrast, at moderate Re, the drag coefficient can be tuned by nearly an order of magnitude, by varying the permeability, at the same level of porosity and weight conditions. Another important feature of our findings at moderate Re is that the drag coefficient varies nonmonotonically with permeability. Comparing the data in Figs. 9(a) and 9(b), for $\mathrm{Re} \in (10, 60)$ and $\mathrm{Re} \in (400, 800)$, respectively, we observe that the maximum of the drag coefficient is shifted towards smaller values of Da, as Re increases. This observation is in agreement with previous numerical results for 2D porous cylinders in Ref. [19], which are here confirmed through precision experiments and over a more detailed range of parameters.

In conclusion, our study suggests a set of guidelines for adjusting the fluid-structure interaction of flexible porous structures at low to moderate Reynolds numbers. In particular, at low Re, permeability has a small influence on the drag coefficient of porous strips, similarly to the rigid case. This observation relaxes some design constraints for light-weight porous structure since its permeability can be regarded as a free parameter that can be set to simplify fabrication. For moderate Reynolds numbers, inertia becomes important and the flow is sufficiently energetic to pass through the holes, thus producing a drop of the drag coefficient for large permeabilities. Therefore, in this moderate Re regime, permeability plays a major role in setting the drag coefficient of the structure. Consequently, for the same weight conditions, the drag coefficient can be tuned by up to an order of magnitude or, *vice versa*, for a required drag coefficient, the mass can be reduced

by a great amount at the cost of requiring a fine microstructure. These findings could be useful for the design of porous flexible flying devices such as microdrones [40], where power consumption is largely affected by weight. On the other hand, this study does not end up providing a quantitative measure of reconfiguration due to the lack of an independent measure of the drag force via, say, a load cell. This challenge is due to the small magnitude of the forces involved (of the order of 10^{-6} N as estimated by the elastica model). Towards a complete understanding of reconfiguration at low Reynolds, future research efforts should aim at measuring drag forces via load cells while extracting the deformed shape of the structures. These efforts would be important in developing a more fundamental understanding of the fluid-structure interactions of insects with porous wings. We hope that the findings presented in this study, together with the questions that it has raised, will motivate further work in these directions.

ACKNOWLEDGMENTS

We thank Hussain H. Karimi for fruitful discussions at the early stages of this work on the theoretical modeling, Paul Grandgeorge for his experimental advice, and Vivek Subramanian for his valuable help with tips on the microfabrication procedure.

APPENDIX A: DETERMINATION OF THE VISCOSITY OF THE FLUIDS USED

In the present study, we used three different viscous fluids for the towing experiments in the fluid tank: (a) distilled water with a dynamic viscosity of $\mu_a = 1.002$ mPa s and a density $\rho_a = 998\ \mathrm{kg/m^3}$ at $T = 20\,^\circ\mathrm{C}$ [41]; (b) a silicone oil (BlueSil 47V1000, Siltech) with a dynamic viscosity on the order of $\mu_b \sim 1$ Pa s and a density of $\rho_b = 970\ \mathrm{kg/m^3}$, and (c) a second silicone oil (BlueSil 47V10, Siltech) with a dynamic viscosity on the order of $\mu_c \sim 10^{-2}$ Pa s and a density of $\rho_c = 950\ \mathrm{kg/m^3}$. The dynamic viscosity of distilled water was obtained from tables in Ref. [41] and that of the two oils was measured experimentally as functions of temperature T, using a rheometer (HR-2, TA Instruments) with a 40 mm aluminum cone with an angle of 2°. The shear rate was fixed at $1\ \mathrm{s^{-1}}$, which was estimated to be comparable to the shear rates encountered in the experiments, and the oil temperature was decreased from 35 °C to 15 °C.

The results of the measurements are plotted in Fig. 12, for both silicone oils in a logarithmic scale. Both measurements show a decreasing viscosity with the temperature, with $\mu_b \in [0.88, 1.15]$ Pa s and $\mu_c \in [0.009, 0.012]$ Pa s, in the temperature range $[15, 35]\,^\circ\mathrm{C}$. This data is then reported in a table provided to our LabView code so that, at each experimental run, the measurements of temperature coming from the thermometer allow the code to search and store the viscosity of the fluid associated to that experimental run. This step is crucial in eliminating uncertainties in the viscosity coming from fluctuations of the temperature, especially for the experiments at low Re where viscosity is directly related to the drag coefficient.

APPENDIX B: DEGREE OF SWELLING OF SILICONE ELASTOMER VPS 32 IN THE SILICONE OILS USED

As detailed in Sec. II C, the porous strips used in the towing experiments were fabricated with a silicone elastomer (VPS). After curing, these strips swell once immersed in a silicone oil bath (but not in water) [42]. To take into account any variations of the geometry due to this swelling and establish their equilibrium shape, we performed free swelling experiments of the porous strip with $i = 1$ (i.e., with hole size $R_1 = 1.429$ mm) in the two oils. At time intervals adjusted according to the speed of the swelling (starting from one measurement every 20 min and then increasing the duration of the intervals as the process slowed down), the strip was taken out of the silicone oil bath and imaged via a camera (Nikon D850) so as to measure its swollen width and length, and returned back in the bath. We then defined the linear swelling ratio λ as the mean between the linear swelling ratio along the width and the one along the length, which could differ from each other by

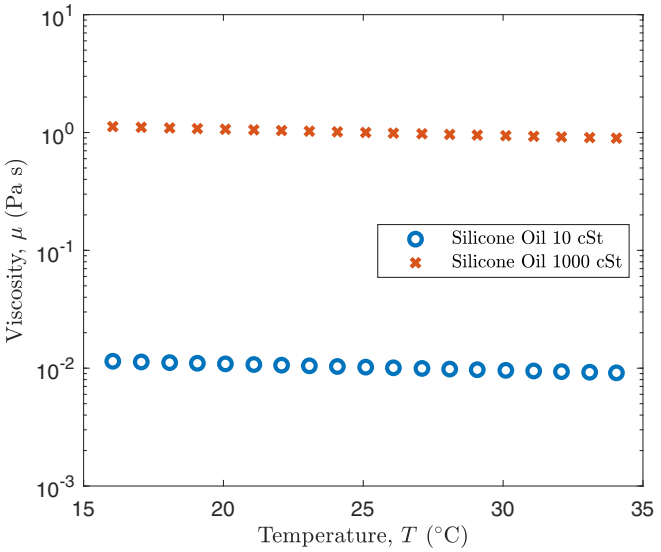

FIG. 12. Dynamic viscosity as a function of temperature for silicone oils BlueSil 47V1000 and BlueSil 47V10.

up to 3%. The results for the free swelling experiments in the two oils are plotted in Fig. 13, where we can notice how the steady-state linear swelling ratio is much larger when the strip is immersed in silicone oil 10 cSt than silicone oil 1000 cSt, reaching a value of $\lambda_c = 1.25$ for the former and a value of $\lambda_b = 1.035$ for the latter. Furthermore, we can observe how the swelling is faster in the less viscous oil, since diffusivity is inversely proportional to viscosity [42]. Error bars represent the

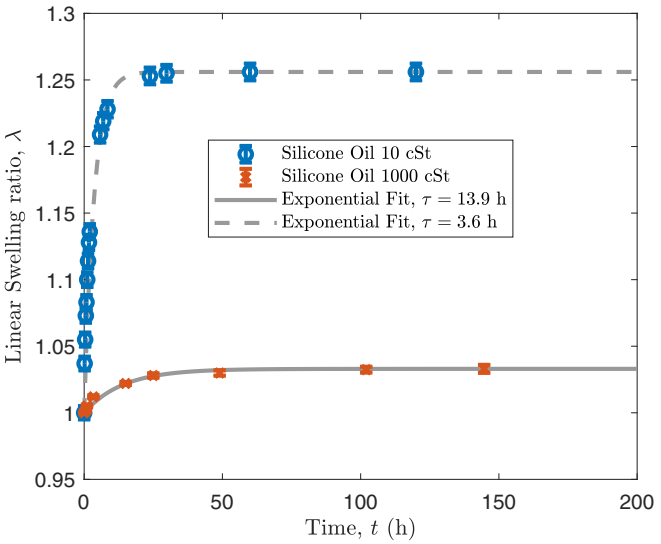

FIG. 13. Linear swelling ratios of a porous strip made of silicone elastomer VPS 32 after having been immersed in the two silicone oils used in this study. The swelling in the less viscous oil (blue symbols) is faster since diffusivity is inversely proportional to viscosity. Gray curves represent fitting via the exponential function in Eq. (B1).

experimental uncertainties originating from the measurements of the swollen lengths and widths, whereas gray curves correspond to fitting via the following exponential function

$$\lambda(t) = \lambda_\infty(1 - e^{-t/\tau}), \tag{B1}$$

with $\tau = 3.6$ h for silicone oil 10 cSt and $\tau = 13.9$ h for silicone oil 1000 cSt. Informed by these results on swelling, we let the strips swell to their steady state before performing any towing experiments, thus eliminating any possible variation in the geometry during an experiment.

All the lengths of our samples have been therefore multiplied by the steady-state linear swelling ratios, depending on which oil they were immersed in. Moreover, swelling produces a variation of the density of the elastomer since a portion of the oil, which has a different density of the elastomer, gets absorbed into the elastomer matrix. Denoting the volumetric swelling ratio as $J = \lambda^3$, the initial volume of the elastomer as V_0, and the volume of the fluid absorbed by V_f, the incompressibility of the phases leads to $V_0 + V_\mathrm{f} = JV_0$. Then, we can compute the density of the swollen elastomer as

$$\rho_\mathrm{s} = \frac{\rho V_0 + \rho_\mathrm{f} V_\mathrm{f}}{JV_0} = \frac{\rho + \rho_\mathrm{f}(J-1)}{J}. \tag{B2}$$

In conclusion, in our elastica models presented in Sec. II D via Eq. (6) and in Sec. III via Eq. (11), we rescaled the density of the elastomer ρ with the density of the swollen elastomer ρ_s, depending on the fluid used. Specifically, the density of the silicone elastomer decreased from 1460 kg/m^3 to 1213 kg/m^3, when swollen in silicone oil 10 cSt, and to 1412 kg/m^3, when swollen in silicone oil 1000 cSt.

[1] J. S. Wexler, P. H. Trinh, H. Berthet, N. Quennouz, O. du Roure, H. E. Huppert, A. Lindner, and H. A. Stone, Bending of elastic fibres in viscous flows: The influence of confinement, J. Fluid Mech. **720**, 517 (2013).

[2] S. A. Combes and T. L. Daniel, Flexural stiffness in insect wings I. Scaling and the influence of wing venation, J. Exp. Biol. **206**, 2979 (2003).

[3] S. K. Jones, Y. J. J. Yun, T. L. Hedrick, B. E. Griffith, and L. A. Miller, Bristles reduce the force required to 'fling' wings apart in the smallest insects, J. Exp. Biol. **219**, 3759 (2016).

[4] H. Wagner, M. Weger, M. Klaas, and W. Schröder, Features of owl wings that promote silent flight, Interface Focus **7**, 20160078 (2017).

[5] E. Lauga, Bacterial hydrodynamics, Annu. Rev. Fluid Mech. **48**, 105 (2016).

[6] M. Piñeirua, B. Thiria, and R. Godoy-Diana, Modelling of an actuated elastic swimmer, J. Fluid Mech. **829**, 731 (2017).

[7] J. Zhang, S. Childress, A. Libchaber, and M. Shelley, Flexible filaments in a flowing soap film as a model for one-dimensional flags in a two-dimensional wind, Nature (London) **408**, 835 (2000).

[8] S. Alben, M. Shelley, and J. Zhang, Drag reduction through self-similar bending of a flexible body, Nature (London) **420**, 479 (2002).

[9] E. de Langre, Effects of wind on plants, Annu. Rev. Fluid Mech. **40**, 141 (2008).

[10] L. Wang, R. Quant, and A. Kolios, Fluid structure interaction modelling of horizontal-axis wind turbine blades based on CFD and FEA, J. Wind Eng. Ind. Aerod. **158**, 11 (2016).

[11] R. H. Scanlan, The action of flexible bridges under wind, I: Flutter theory, J. Sound Vib. **60**, 187 (1978).

[12] M. Drela, *Flight Vehicle Aerodynamics* (MIT Press, Cambridge, MA, 2014).

[13] M. P. Païdoussis, P. S. J., and E. de Langre, *Fluid-Structure Interactions: Cross-Flow-Induced Instabilities* (Cambridge University Press, Cambridge, 2014).

[14] H. Darcy, Les fontaines publique de la ville de Dijon, Dalmont, Paris **647**, 1 (1856).

[15] H. C. Brinkman, A calculation of the viscous force exerted by a flowing fluid on a dense swarm of particles, Appl. Sci. Res. **1**, 27 (1949).

[16] D. N. Sutherland and C. T. Tan, Sedimentation of a porous sphere, Chem. Eng. Sci. **25**, 1948 (1970).

[17] J. H. Masliyah and M. Polikar, Terminal velocity of porous spheres, Can. J. Chem. Eng. **58**, 299 (1980).
[18] R. P. Roger and R. G. Hussey, Stokes drag on a flat annular ring, Phys. Fluids **25**, 915 (1982).
[19] P. D. Noymer, L. R. Glicksman, and A. Devendran, Drag on permeable cylinder in steady flow at moderate Reynolds numbers, Chem. Eng. Sci. **53**, 2859 (1998).
[20] I. P. Castro, Wake characteristics of two-dimensional perforated plates normal to an air-stream, J. Fluid Mech. **46**, 599 (1971).
[21] C. Cummins, I. M. Viola, E. Mastropaolo, and N. Nakayama, The effect of permeability on the flow past permeable disks at low Reynolds numbers, Phys. Fluids **29**, 097103 (2017).
[22] P. G. Ledda, L. Siconolfi, F. Viola, F. Gallaire, and S. Camarri, Suppression of von Kármán vortex streets past porous rectangular cylinders, Phys. Rev. Fluids **3**, 103901 (2018).
[23] P. C. Carman, The determination of the specific surface of powders, J. Soc. Chem. Ind. **57**, 225 (1938).
[24] P. C. Carman, *Flow of Gases through Porous Media* (Academic Press, New York, 1956).
[25] A. M. Jones, Drag coefficients for flat plates, spheres, and cylinders moving at low Reynolds numbers in a viscous fluid, Master's thesis, Oregon State College (1958).
[26] E. F. Strong, M. Pezzulla, F. Gallaire, P. Reis, and L. Siconolfi, Hydrodynamic loading of perforated disks in creeping flows, Phys. Rev. Fluids **4**, 084101 (2019).
[27] K. H. Jensen, A. X. C. N. Valente, and H. A. Stone, Flow rate through microfilters: Influence of the pore size distribution, hydrodynamic interactions, wall slip, and inertia, Phys. Fluids **26**, 052004 (2014).
[28] Y. Jin, J.-T. Kim, S. Cheng, O. Barry, and L. P. Chamorro, On the distinct drag, reconfiguration and wake of perforated structures, J. Fluid Mech. **890**, A1-1 (2020).
[29] M. Guttag, H. H. Karimi, C. Falcón, and P. M. Reis, Aeroelastic deformation of a perforated strip, Phys. Rev. Fluids **3**, 014003 (2018).
[30] Z. Dagan, S. Weinbaum, and R. Pfeffer, An infinite-series solution for the creeping motion through an orifice of finite length, J. Fluid Mech. **115**, 505 (1982).
[31] K. Steiros and M. Hultmark, Drag on flat plates of arbitrary porosity, J. Fluid Mech. **853**, R3 (2018).
[32] F. Gosselin, E. de Langre, and B. A. Machado-Almeida, Drag reduction of flexible plates by reconfiguration, J. Fluid Mech. **650**, 319 (2010).
[33] B. Audoly and Y. Pomeau, *Elasticity and Geometry: From Hair Curls to the Non-linear Response of Shells* (Oxford University Press, Oxford, 2010).
[34] J.-K. Lee and J.-G. Kim, An analytical study on prediction of effective elastic constants of perforated plate, J. Mech. Sci. Technol. **19**, 2224 (2005).
[35] P. Buchak, C. Eloy, and P. M. Reis, The Clapping Book: Wind-Driven Oscillations in a Stack of Elastic Sheets, Phys. Rev. Lett. **105**, 194301 (2010).
[36] Camille Duprat and Howard Stone, editors, *Fluid-Structure Interactions in Low-Reynolds-Number Flows*, Soft Matter Series, Vol. 4 (Royal Society of Chemistry, London, 2016).
[37] M. J. Lighthill, Note on the swimming of slender fish, J. Fluid Mech. **9**, 305 (1960).
[38] A. Y. L. Cheer and M. A. R. Koehl, Paddles and rakes: Fluid flow through bristled appendages of small organisms, J. Theor. Biol. **129**, 17 (1987).
[39] S. Vogel, Drag and reconfiguration of broad leaves in high winds, J. Exp. Bot. **40**, 941 (1989).
[40] N. T. Jafferis, E. F. Helbling, M. Karpelson, and R. J. Wood, Untethered flight of an insect-sized flapping-wing microscale aerial vehicle, Nature (London) **570**, 491 (2019).
[41] M. L. Huber, R. A. Perkins, A. Laesecke, D. G. Friend, J. V. Sengers, M. J. Assael, I. N. Metaxa, E. Vogel, R. Mareš, and K. Miyagawa, New international formulation for the viscosity of H_2O, J. Phys. Chem. Ref. Data **38**, 101 (2009).
[42] J. N. Lee, C. Park, and G. M. Whitesides, Solvent compatibility of poly(dimethylsiloxane)-based microfluidic devices, Anal. Chem. **75**, 6544 (2003).